

Dust Size Growth and Settling in a Protoplanetary Disk

Hideko Nomura and Yoshitsugu Nakagawa

Department of Earth and Planetary Sciences, Kobe University, Kobe 657-8501, Japan

hnomura@kobe-u.ac.jp, yoshi@kobe-u.ac.jp

ABSTRACT

We have studied dust evolution in a quiescent or turbulent protoplanetary disk by numerically solving coagulation equation for settling dust particles, using the minimum mass solar nebular model. As a result, if we assume an ideally quiescent disk, the dust particles settle toward the disk midplane to form a gravitationally unstable layer within 2×10^3 – 4×10^4 yr at 1–30 AU, which is in good agreement with an analytic calculation by Nakagawa, Sekiya, & Hayashi (1986) although they did not take into account the particle size distribution explicitly. In an opposite extreme case of a globally turbulent disk, on the other hand, the dust particles fluctuate owing to turbulent motion of the gas and most particles become large enough to move inward very rapidly within 70 – 3×10^4 yr at 1–30 AU, depending on the strength of turbulence. Our result suggests that global turbulent motion should cease for the planetesimal formation in protoplanetary disks.

Subject headings: dust dynamics — planetary systems: formation — planetary systems: protoplanetary disks

1. Introduction

It is believed that particle settling and growth are important processes leading to the planet formation in protoplanetary disks. Observationally some evidences of dust size growth have been proposed based on dust continuum emission from the protoplanetary disks, such as smaller power-law indices of spectral energy distributions (SEDs) in sub-mm to cm wavelength bands, and fainter trapezium feature of $10\mu\text{m}$ silicate emission, compared with those of the interstellar dust grains (e.g., Beckwith & Sargent 1991; Miyake & Nakagawa 1993;

Beckwith et al. 2000; Kitamura et al. 2002; van Boekel et al. 2003; Przygodda et al. 2003; Wilner et al. 2005). Meanwhile, theoretically the initial stage of dust evolution when micron-sized interstellar dust particles grow into centimeter-sized particles with settling toward the disk midplane have been studied analytically and numerically; for example, Weidenschilling (1980) and Nakagawa et al. (1981, 1986)’s works in a quiescent disk, and Cuzzi et al. (1993) and Weidenschilling (1997, 2004)’s works in local turbulence induced by the shear between the dust layer and the gas near the disk midplane (see also Weidenschilling & Cuzzi 1993 and references therein).

In addition to the shear-induced turbulence, it is thought that there exists global turbulent motion in the protoplanetary disks, which is caused by thermal convective and/or magneto-rotational instabilities (e.g., Lin & Papaloizou 1980; Balbus & Hawley 1991). The turbulent motion of the gas is known to affect the dust evolution processes; turbulence induced relative motion increases the mutual collision rate, that is, the growth rate of the dust particles (e.g., Völk et al. 1980), turbulent mixing motion lets the particles move diffusively (e.g., Cuzzi et al. 1993), and turbulent eddies trap the dust particles (e.g., Klahr & Henning 1997; Cuzzi et al. 2001; Johansen et al. 2004). On the other hand, the disk instabilities, namely, the existence of turbulent regions depend on the spatial and size distributions of the dust particles (e.g., Mizuno et al. 1988; Sano et al. 2000; Nomura 2004). Therefore, self-consistent treatment of the evolution of the dust particles and the turbulent regions (the disk instabilities) is needed in order to understand the very beginning of planet formation process in protoplanetary disks before the dust particles settle toward the disk midplane and form a dusty layer, which could lead to the planetesimal formation.

Moreover, recent observations have been providing a huge amount of data of spectra and SEDs of dust continuum emission as well as molecular line emissions from protoplanetary disks. Theoretically reproducing these observational data have been also developed using detailed disk models (e.g., Kenyon & Hartmann 1987; Miyake & Nakagawa 1995; Chiang & Goldreich 1997; D’Alessio et al. 1998; Dullemond et al. 2001; van Zadelhoff et al. 2001; Aikawa et al. 2002; Nomura & Millar 2005). Although rather simple dust models have been used in those previous models, the dust properties affect the physical and chemical structure of the disks, and then the observable properties very much (e.g., D’Alessio et al. 2001; Aikawa & Nomura 2005). Thus, we should carefully model the dust evolution in the disks and compare the model predictions with the observational data in order to interpret the observations and understand what is actually going on in protoplanetary disks. The SEDs of young stellar objects have been tried to be modeled by numerically simulating the dust size growth and settling processes in the disks (Suttner & Yorke 2001; Tanaka et al. 2005; Dullemond & Dominik 2005).

In this paper, we have studied basic behavior of dust evolution in a quiescent or globally turbulent protoplanetary disk, especially focusing on time scales and growing dust size. It is done by numerically solving the coagulation equation, using a simple disk model, as a first step of understanding the initial stage of planet formation and modeling observational properties of protoplanetary disks. In the following section, we present the disk model as well as the basic equations for the vertical and radial motion and the coagulation of dust particles. In §3, we numerically calculate the dust size growth and settling toward the midplane in a quiescent disk, and compare the result with that obtained analytically by Nakagawa et al. (1986; hereafter NSH86). We also discuss the dust evolution in a globally turbulent disk in §4. Finally, the results are summarized in §5.

2. Basic Equations and Models

2.1. Disk Model

As a disk model, we adopt the minimum mass solar nebular model (e.g., Safronov 1969; Hayashi 1981; Hayashi et al. 1985) in order to examine basic behavior of the dust evolution under a simple physical condition of the gas and compare the results with analytic calculation (see §3). In this model the gas surface density profile is given by

$$\Sigma_{\text{gas}} = 1.7 \times 10^3 (R/\text{AU})^{-3/2} \text{g cm}^{-2}, \quad (1)$$

where R is the radial distance from the central star. The surface density of dust particles is

$$\Sigma_{\text{dust}} = \left\{ \begin{array}{c} 7.1 \\ 30 \end{array} \right\} (R/\text{AU})^{-3/2} \text{g cm}^{-2} \quad \text{for} \quad \left\{ \begin{array}{l} R < 2.7 \text{AU} \\ R > 2.7 \text{AU} \end{array} \right., \quad (2)$$

where the solid density of a dust particle, ρ_s , is set to be $\rho_s = 2$ and 1 g cm^{-3} for $R < 2.7 \text{ AU}$ and $R > 2.7 \text{ AU}$, respectively, taking into account the effect of water ice sublimation. We note that each of the mass and the surface density distribution is one of the most unknown factors in modeling protoplanetary disks. Numerical calculation of dust evolution using some different parameters for the disk mass and the power-law index of the surface density distribution as a function of the radial distance is performed by Tanaka et al. (2005). The dust and gas temperature is given by

$$T = 280(R/\text{AU})^{-1/2} \text{K}. \quad (3)$$

In this paper we treat the region where the vertical distance from the disk midplane, Z , is smaller than the disk scale height,

$$H = (\sqrt{\pi}/2)(c_s/\Omega_K) = 0.0472(R/\text{AU})^{5/4} \text{AU}, \quad (4)$$

where $c_s = (8kT/\pi m_\mu)^{1/2}$ ($m_\mu = 2.34m_H$ is the mean molecular mass and m_H the mass of an atomic hydrogen) is the mean thermal velocity and $\Omega_K = (GM_*/R^3)^{1/2}$ (G is the gravitational constant and M_* the mass of the central star) is the Keplerian frequency. And we simply assume that the profiles of the temperature (eq. [3]) and the gas density,

$$\rho_{\text{gas}} = \Sigma_{\text{gas}}/\sqrt{\pi}H = 1.36 \times 10^{-9}(R/\text{AU})^{-11/4} \text{g cm}^{-3}, \quad (5)$$

are uniform in the vertical direction. The mass of the central star is assumed to be $M_* = 1M_\odot$.

2.2. Equations of Motion of Dust Particles and Gas

The equations of motion of dust particles and gas in the disk are given by

$$\frac{d\mathbf{U}}{dt} = -A\rho_{\text{gas}}(\mathbf{U} - \mathbf{u}) - \frac{GM_*}{R^3}\mathbf{R}, \quad (6)$$

and

$$\frac{d\mathbf{u}}{dt} = -A\rho_{\text{dust}}(\mathbf{u} - \mathbf{U}) - \frac{GM_*}{R^3}\mathbf{R} - \frac{\nabla p_{\text{gas}}}{\rho_{\text{gas}}}, \quad (7)$$

where \mathbf{U} and \mathbf{u} are the velocities of dust and gas particles in the inertial frame of reference, and ρ_{dust} the spatial mass density of dust particles, p_{gas} the gas pressure. The drag coefficient, A , is given by

$$A = \begin{cases} c_s/\rho_s a & \text{for } a \lesssim l_g, \\ 3c_s l_g/2\rho_s a^2 & \text{for } a \gtrsim l_g, \end{cases} \quad (8)$$

following Epstein's and Stokes' law (Epstein 1924; Stokes 1851), respectively. The symbol a is the radius of the dust particles and l_g is the mean free path of the gas particles, given by $l_g = m_\mu/(\sigma_{\text{mol}}\rho_{\text{gas}}) = 1.44(R/\text{AU})^{11/4} \text{cm}$, where $\sigma_{\text{mol}} = 2 \times 10^{-15} \text{cm}^2$ is the molecular cross section. The shape of the dust particles is simply assumed to be a compact sphere in this paper. We note that the dust shape (mass/area ratio) affects the dust evolution through the drag coefficient and the sticking rate (see next subsection), and many numerical studies have dealt with the effects of the dust shape, taking into account fractal structure of dust aggregates (e.g., Weidenschilling & Cuzzi 1993; Ossenkopf 1993; Weidenschilling 1997; Suttner & Yorke 2001; Dullemond & Dominik 2005).

Now, we assume that the disk is axisymmetric and rotates around the central star at nearly Keplerian velocity, and set the dust and gas velocities relative to the Keplerian velocity, $\mathbf{v}_K (= R\Omega_K\hat{\phi})$, as $\mathbf{V} = \mathbf{U} - \mathbf{v}_K$ and $\mathbf{v} = \mathbf{u} - \mathbf{v}_K$. As far as the dust particles are small enough, the timescale for initial velocity of dust particles decaying due to the gas drag force is much shorter than the Keplerian time and the timescale of collision between dust particles

(e.g., Nakagawa et al. 1981). Thus, the mean motion of dust particles becomes steady soon in a quiescent disk (see also §4.1). By setting $\partial/\partial t = 0$ in the equations of motion, we can derive the terminal velocities of the vertical and radial motion of dust particles as

$$V_Z - v_Z = -(\Omega_K^2/D_g)Z, \quad (9)$$

where $D_g = A\rho_{\text{gas}}$, and

$$V_R - v_R = -\frac{2D\Omega_K}{D^2 + \Omega_K^2}\eta v_K \quad \text{and} \quad V_R = -\frac{\rho_{\text{gas}}}{\rho_{\text{gas}} + \rho_{\text{dust}}}\frac{2D\Omega_K}{D^2 + \Omega_K^2}\eta v_K, \quad (10)$$

where $D = A(\rho_{\text{gas}} + \rho_{\text{dust}})$ and

$$\eta = -\frac{1}{2R\Omega_K^2}\frac{1}{\rho_{\text{gas}}}\frac{\partial p_{\text{gas}}}{\partial R} = 1.81 \times 10^{-3}(R/\text{AU})^{1/2} \quad (11)$$

(see NSH86 for details).

2.3. Coagulation Equation for Settling Particles

We solve the following dispersed coagulation equation numerically for simulating the size growth of settling dust particles in the disk, according to Nakagawa et al. (1981) and Nakagawa & Kohno (1999);

$$\frac{\partial \varphi(i)}{\partial t} + \frac{\partial}{\partial Z}[V_Z(i)\varphi(i)] = -m_i\varphi(i)\sum_{j=1}^n \beta(i,j)\varphi(j) + \frac{1}{2}m_i\sum_{j=1}^{i-1} \beta(i-j,j)\varphi(i-j)\varphi(j), \quad (12)$$

where

$$\varphi(i) = \int_{m_{i-1/2}}^{m_{i+1/2}} \rho(m)dm \quad (13)$$

is the mass density of the dust particles whose mass ranges from $m_{i-1/2}$ to $m_{i+1/2}$, and $m_i = (m_{i-1/2} + m_{i+1/2})/2$ for $i = 1, \dots, n$. The dust mass is binned into n intervals logarithmically as $m_{i+1/2} = \varepsilon m_{i-1/2}$, where $m_i = (4\pi/3)\rho_s a_i^3$ (the dust particles are assumed to have a shape of compact sphere), $a_1 = 1\mu\text{m}$, $n = 320$, and $\varepsilon = \sqrt[4]{2}$ are adopted in this paper (see Appendix). Here, the total mass density of dust particles at a given position and time is given by

$$\rho_{\text{dust}} = \int_{m_{1/2}}^{m_{n+1/2}} \rho(m)dm = \sum_{i=1}^n \varphi(i). \quad (14)$$

The second term of the left hand side of equation (12) shows the mass transport of dust particles in the vertical direction. Now, the mean vertical velocity of the gas is negligible

($v_z \approx 0$), so the dust particles settle toward the disk midplane. The mean settling velocity of dust particles with mass m_i is derived as $V_Z(i) = -(\rho_{\text{gas}}c_s/\rho_s a_i)\Omega_K^2 Z$ (if $a_i \lesssim l_g$) or $-(3\rho_{\text{gas}}c_s l_g/2\rho_s a_i^2)\Omega_K^2 Z$ (if $a_i \gtrsim l_g$) from equations (8) and (9). In a turbulent disk the dust particles are transported by turbulent mixing in addition (see §4.3). The mass transport of dust particles in the radial direction is not solved in this paper for simplicity.

The symbol $\beta(i, j)$ is related to the sticking rate of two colliding dust particles, and given by

$$\beta(i, j) = \pi(a_i + a_j)^2 \delta V p_s / m_i m_j, \quad (15)$$

where we simply assume the sticking probability of $p_s = 1$ in this paper. We note that the sticking probability will depend on size, relative velocities, chemical composition and/or shape of dust grains (e.g., Weidenschilling & Cuzzi 1993; Weidenschilling 2004; see also references therein). Lower probability will make the timescale of the dust evolution longer (e.g., Tanaka et al. 2005). Here, we neglect fragmentation of dust particles, which could occur if the particles become large and their relative velocities with small particles become high enough (e.g., Dullemond & Dominik 2005). As the relative velocity between the dust particles, δV , we take into account the thermal Brownian motion,

$$\delta V_B = \left(\frac{8kT}{\pi}\right)^{1/2} \left(\frac{1}{m_i} + \frac{1}{m_j}\right)^{1/2}, \quad (16)$$

where k is Boltzmann's constant, and the velocity differences in the vertical and radial directions, $\delta V_Z = V_Z(i) - V_Z(j)$ and $\delta V_R = V_R(i) - V_R(j)$, which are derived from equations (9) and (10), respectively. The azimuthal velocity difference, δV_ϕ , has very weak size dependence as far as the dust particles are small (e.g., NSH86); hence we neglect δV_ϕ . We adopt the relative velocity of $\delta V = (\delta V_B^2 + \delta V_Z^2 + \delta V_R^2)^{1/2}$ in a quiescent disk. In a turbulent disk we take into account the turbulence induced relative velocity, δV_t , in addition as $\delta V = (\delta V_B^2 + \delta V_Z^2 + \delta V_R^2 + \delta V_t^2)^{1/2}$ (see §4.3).

In our numerical calculation the spatial grid in the vertical direction is taken equally spaced into 20 intervals within $0 < Z < H$. In addition, within the lowest interval of $0 < Z < H/20$, we take logarithmically spaced 17 sub-intervals as $Z_{l+1} = 2Z_l$ in order to resolve the region near the disk midplane in a quiescent disk. In a turbulent disk only equally spaced 20 intervals within $0 < Z < H$ are used without sub-intervals because the dust size distributions are almost identical between the lowest vertical disk layers and the calculation of the diffusive mass transport due to the turbulent mixing is very time consuming if we use such small spatial sub-grids (see §4.3).

3. Dust Evolution in a Quiescent Disk

By numerically solving the coagulation equation for settling dust particles (eq. [12]), we obtain the dust size distributions at a given time and disk height at the Earth’s (1AU), Jupiter’s (5.2AU), or Neptune’s (30AU) orbits. As an initial condition, we assume that the dust particles are well-mixed with the gas and have a radius of a certain value, a_{init} . We adopt $a_{\text{init}} = 10, 20, \text{ and } 60 \mu\text{m}$ for $R = 1, 5.2, \text{ and } 30 \text{ AU}$, respectively, in order to compare the numerical results with the analytic calculation by NSH86. These values correspond to the wavelength of the peak emission at the local temperature and do not have particular physical meaning. The initial condition of the dust size distribution, however, does not affect the results very much.

First, we compare our numerical result of the dust settling time with that by NSH86. Figure 1 shows the time evolution of spatial dust mass distribution obtained by our numerical calculation at the orbits of $R =$ (a) 1AU, (b) 5.2AU, and (c) 30AU. The vertical axis represents the dust surface density from $Z = 0$ to a characteristic height $Z = Z_k$ ($k = 1, \dots, 4$) at R , $\Sigma(Z < Z_k) = \int_{-Z_k}^{Z_k} \rho_{\text{dust}}(R, Z) dZ$, divided by the total dust surface density there, Σ_{dust} (eq.[2]). The values, $Z_1, Z_2, Z_3, \text{ and } Z_4$, at $R = 1, 5.2, \text{ and } 30 \text{ AU}$ are listed in Table 1. These characteristic heights are defined in NSH86 (see Fig.1 of NSH86); to put it briefly, the vertical velocity, V_Z (eq. [9]), of dust particles dominates the radial velocity, V_R (eq. [10]), above $Z = Z_1$, and the gas density, ρ_{gas} , is larger than the dust density, ρ_{dust} , above $Z = Z_2$. The vertical velocity, V_Z , dominates the radial velocity, V_R , again below $Z = Z_3$ where the dust density is high enough that the gas drag force hardly affects the radial motion of the dust particles. If most dust particles settle below $Z = Z_4$, the dust layer becomes gravitationally unstable and could fragment into planetesimals. The dashed, dotted, dot-dashed, and solid lines in Figure 1 represent the dust surface density below $Z = Z_1, Z_2, Z_3, \text{ and } Z_4$, respectively. As time goes on, the dust particles settle toward the disk midplane and more mass is included in the lower layer of the disk. In Figure 2 we plot the dust settling time at which 70% of the total dust mass settles below Z_k ($k = 1, \dots, 4$) at the orbits of $R = 1\text{AU}$ (squares), 5.2AU (circles), and 30AU (diamonds). Together with them, the dust settling time obtained by NSH86 is also plotted (triangles with solid lines). The figure shows that the numerical results are in good agreement with the analytic results, and most dust particles settle below $Z = Z_4$, which leads to the formation of a gravitationally unstable dust layer, within about $2 \times 10^3, 6 \times 10^3, \text{ and } 4 \times 10^4 \text{ yrs}$ at the orbits of $R = 1, 5.2, \text{ and } 30 \text{ AU}$, respectively, in a quiescent disk.

Next, Figure 3 shows the resulting size distributions of mass density of dust particles, $\varphi(i)$, normalized by ρ_{dust} at (a) $R = 1\text{AU}, t = 1 \times 10^3 \text{ yr}$, (b) $R = 1\text{AU}, t = 2 \times 10^3 \text{ yr}$; (c) $R = 5.2\text{AU}, t = 3 \times 10^3 \text{ yr}$, (d) $R = 5.2\text{AU}, t = 6 \times 10^3 \text{ yr}$; (e) $R = 30\text{AU}, t = 1 \times 10^4 \text{ yr}$,

and (f) $R = 30\text{AU}$, $t = 4 \times 10^4$ yr. The dashed, dotted, dot-dashed, and solid lines in each figure represent the size distributions at the characteristic heights, $Z = Z_1, Z_2, Z_3$, and Z_4 , respectively. The time used in Figure 3*a*, *c*, and *e* corresponds to $t = t_1$ and that in Figure 3*b*, *d*, and *f* corresponds to $t = t_4$, where t_k denotes the time at which 70% of the dust particles settle below the characteristic height, $Z = Z_k$, at each orbit, R (see Fig. 2). Now, we can see from Figure 3 that the larger dust particles which have grown at the disk surface layer settle more rapidly toward the midplane with growing larger and larger. These processes lead to a bimodal size distribution near the midplane at the inner disk (e.g., Weidenschilling 1997). The gaps appear in Figure 3*a* and *b* around $a = l_g = 1$ cm where the drag coefficient, A (eq.[8]), begins to follow Stokes' law, rather than Epstein's law. The drag coefficient always follows Epstein's law at $R = 5.2$ and 30AU in this model, where l_g is much larger ($l_g = 1 \times 10^2$ and 2×10^4 cm, respectively). The timescale of the dust size growth and settling is shorter at the inner disk where the effect of gravitational force of the central star is stronger.

Finally, we compare our numerical result of the evolution of dust particle radius with that by NSH86. In Figure 4 we plot the resulting largest dust radii at $Z = Z_k$ ($k = 1, \dots, 4$) and $R = 1\text{AU}$ (squares), 5.2AU (circles), and 30AU (diamonds). The largest dust radii, a_{max} , at $Z = Z_k$ are obtained applying a criterion, $i_{\text{max}} = \max\{i \mid \varphi(i)/\rho_{\text{dust}} > 10^{-8}\}$, to the dust size distribution at $t = t_k$ (cf. thin solid lines in Fig. 3). The evolution of dust radii obtained by NSH86 is also plotted (triangles with solid lines). The figure shows that the numerical results are in good agreement with the analytic results within a factor of two, except at $Z = Z_1$. The dust radii at $Z = Z_1$ are larger in the numerical calculation because the relative velocity between dust particles due to the thermal Brownian motion, which works efficiently for small dust particles, is taken into account in the numerical calculation, but not in the analytic calculation in NSH86. Both numerical and analytic calculations show that the dust particles grow and their radii finally reach about 20, 7, and 1 cm at the orbits of $R = 1, 5.2$, and 30 AU, respectively, just before they settle below $Z = Z_4$.

We note that the orbital decay is very little in a quiescent disk; during settling from $Z = H$ to $Z = Z_4$, the dust particles move radially by $\Delta R = 2.2 \times 10^{-3}$, 0.20, and 2.8AU at the orbits of $R = 1, 5.2$, and 30AU , respectively, according to NSH86.

Here it should be commented that although we simply assume a totally quiescent disk in this section, in reality it is expected that the shear between the dust layer and the gas induces turbulence locally near the midplane as the dust particles settle (e.g., Cuzzi et al. 1993; Weidenschilling & Cuzzi 1993; Weidenschilling 1997; Cuzzi & Weidenschilling 2005). Actually if we compute the Richardson number, $J = -(\partial\rho_{\text{dust}}/\partial Z)(\rho_{\text{gas}} + \rho_{\text{dust}})^{-1}\Omega_K^2 Z(\partial V_\phi/\partial Z)^{-2} = Z(\eta R \rho_{\text{gas}})^{-2}(\rho_{\text{gas}} + \rho_{\text{dust}})^3(\partial\rho_{\text{dust}}/\partial Z)^{-1}$ (e.g., Sekiya 1998; Chandrasekhar 1961), we can find that $J < 0.25$ and the shear instability will occur below $Z = Z_2$ at each orbit. In

such a turbulent layer the dust particles do not concentrate in the midplane and migrate inward very rapidly once they grow large enough as we will see in next section (although it is different in point that this is local turbulence).

In conclusion, our numerical calculation have confirmed that NSH86’s approximate treatment of the dust size growth and settling processes are appropriate for describing the dust settling time and the evolution of the largest dust size in an ideally quiescent disk, although they did not take into account the dust size distribution explicitly. This will be because most dust mass is included in the dust particles with the largest sizes, and the dust settling time is controlled by the largest dust particles which have the highest settling velocity.

4. Dust Evolution in a Turbulent Disk

In this section we discuss the dust evolution in the disk in which global turbulent motion exists induced by, for example, thermal convective and/or magneto-rotational instabilities.

4.1. Vertical Motion

First, we examine the vertical motion of one dust particle, not the mean motion which we have treated in the previous sections. The equation of motion of a dust particle (eq.[6]) in the vertical direction is written as

$$\frac{d^2 Z}{dt^2} = -D_g \left(\frac{dZ}{dt} - u_z \right) - \Omega_K^2 Z. \quad (17)$$

The vertical velocity of the gas in a turbulent medium is generally given by $u_z = \overline{u_z} + u'_z$, where the overline means a time average and the prime is a fluctuation due to the turbulent motion. Now we put the mean velocity to be $\overline{u_z} = 0$ since we assume the hydrostatic equilibrium. As the component of turbulent fluctuation, we simply adopt an oscillating motion of $u'_z = v_t \exp(i\omega_t t)$, which models the motion of the largest turbulent eddy with a velocity v_t and a frequency ω_t ($\omega_t \sim v_t/l_t$ where l_t is the eddy size). In this case, equation (17) has a general solution that consists of a mean motion part, $\overline{Z}(t)$, and a fluctuation part, $Z'(t)$, caused by the turbulent motion of the gas,

$$Z(t) = \overline{Z}(t) + Z'(t), \quad (18)$$

where

$$\overline{Z}(t) = C_1 \exp(\lambda_1 t) + C_2 \exp(\lambda_2 t), \quad (19)$$

and

$$Z'(t) = \frac{D_g v_t \exp[i(\omega_t t - \delta)]}{[(\Omega_K^2 - \omega_t^2)^2 + D_g^2 \omega_t^2]^{1/2}}, \quad \delta = \tan^{-1} \frac{D_g \omega_t}{\Omega_K^2 - \omega_t^2}. \quad (20)$$

In equation (19) C_1 and C_2 are integral constants, and

$$\lambda_{1,2} = -\frac{1}{2}(D_g \pm \sqrt{D_g^2 - 4\Omega_K^2}) \quad (21)$$

$$\simeq \begin{cases} -D_g, & -\Omega_K^2/D_g & \text{for } D_g \gg 2\Omega_K, \\ -(D_g/2) \mp i\Omega_K & & \text{for } D_g \ll 2\Omega_K. \end{cases} \quad (22)$$

If we assume that the eddy turn over frequency is equal to the Keplerian frequency, $\omega_t = \Omega_K$, the fluctuation part (20) becomes $Z'(t) \approx (v_t/c_s)H \exp[i(\Omega_K t - \pi/2)]$, which means that the turbulent gas motion forces the dust particle to continue to oscillate vertically with an amplitude $(v_t/c_s)H$ and a frequency Ω_K , independent of the dust particle size (e.g., Landau et al. 1967). If we think a more realistic case, the turbulent velocity of the gas, u'_z , will be modeled by a superposition of eddies with various sizes, velocities, and frequencies, which is often decomposed into Fourier components (e.g., Landau & Lifshitz 1959). In this case the term for fluctuating motion (20) is also given by a superposition of oscillations with various frequencies. Now, the mean motion part (19) shows the settling of the dust particle toward the disk midplane. From equation (18) we can derive the particle velocity, which also consists of a mean motion, $\bar{V}(t)$, and a fluctuation, $V'(t)$, as

$$V(t) = \bar{V}(t) + V'(t), \quad (23)$$

where $\bar{V}(t) = d\bar{Z}(t)/dt$ and $V'(t) = dZ'(t)/dt$. For a small particle which satisfies $D_g > 2\Omega_K$, we obtain $\bar{Z}(t) \simeq Z_0 \exp[-(\Omega_K^2/D_g)t]$ (Z_0 is the initial value of $\bar{Z}(t)$) and $\bar{V}(t) \simeq -(\Omega_K^2/D_g)\bar{Z}(t)$.

We note that in a quiescent disk in which $u_z = 0$, a general solution of equation (17) is simply given by the mean motion part, $\bar{Z}(t)$, in equation (19). Therefore, the dust particles always settle toward the disk midplane; the motion of a large dust particle which satisfies $D_g < 2\Omega_K$ is oscillation around $Z = 0$, damped (that is, the particle settles toward the disk midplane) with a timescale of $2/D_g$, while a smaller particle ($D_g > 2\Omega_K$) settles with a timescale of D_g/Ω_K^2 without oscillation (e.g., NSH86).

4.2. Radial Motion

Next, we will discuss the radial motion of the dust particles in a turbulent disk. When the dust particles are small enough, their motion is strongly coupled with the turbulent gas

motion. If the particles grow and reach a critical radius, they are released from the turbulent eddy trapping and migrate toward the central star (see e.g., Klahr & Henning 1997 for more detailed description of the dust particle motion in a turbulent eddy). The critical radius, a_{crit} , is roughly estimated by comparing the friction time between the gas and dust particles, $\tau_f = 1/D_g$, with the turnover time of the largest turbulent eddy, $\tau_{\text{eddy}} = 1/\Omega_K$, and given by

$$a_{\text{crit}} = \begin{cases} c_s \rho_{\text{gas}} / \rho_s \Omega_K & \text{for } a \lesssim l_g, \\ (3c_s \rho_{\text{gas}} l_g / 2\rho_s \Omega_K)^{1/2} & \text{for } a \gtrsim l_g. \end{cases} \quad (24)$$

The critical radii at $R = 1, 5.2,$ and 30AU are $a_{\text{crit}} = 32, 80,$ and 6 cm, respectively. When the dust radius reaches a_{crit} and the friction time, τ_f , becomes as long as the eddy turnover time, τ_{eddy} , the radial velocity of the particle becomes the maximum, $V_R \simeq \eta v_K = 5 \times 10^3 \text{cm s}^{-1}$ (see eq. [10]), and the particle migrates inward very rapidly with the timescales of $R/V_R \simeq 1 \times 10^2, 5 \times 10^2,$ and 3×10^3 yrs at $R = 1, 5.2,$ and 30AU , respectively (e.g., Adachi et al. 1976; Weidenschilling 1977).

4.3. Dust Size Growth in a Turbulent Disk

Next, taking into account the properties of vertical and radial motion of dust particles mentioned in the previous subsections, we will numerically simulate the dust evolution in a turbulent disk by solving the coagulation equation (12). In this simulation we artificially remove the dust particles whose radii reach a_{crit} as they migrate inward very rapidly. Numerical simulation including radial mass transport of the dust particles should be done in future (cf. Weidenschilling 2004).

As we mentioned in §2.3 the relative velocity between the dust particles induced by microscopic motion of the turbulent gas, δV_t , is taken into account in this numerical calculation. As the relative velocity we adopt the approximate treatment by Weidenschilling (1984), which reproduces the result of Völk et al. (1980)'s analysis of the nonlinear response of a dust particles to the turbulent gas motion with a Kolmogorov spectrum. In addition, we use Mizuno et al. (1988)'s formula when the friction time is shorter than the turnover time of the smallest turbulent eddy (see also Markiewicz et al. 1991). The adopted relative velocity is

$$\delta V_t = \begin{cases} \frac{3\tau_{f_j}}{(\tau_{f_i} + \tau_{f_j})} \left(\frac{\tau_{f_j}}{\tau_{k_0}}\right)^{1/2} v_t & \text{for } \tau_{f_i} \leq \tau_{f_j} < \tau_{k_0}, \\ \left(\frac{|\tau_{f_i} - \tau_{f_j}|}{\tau_{f_i} + \tau_{f_j}}\right)^{1/2} \left| \frac{\tau_{f_i}}{\tau_{k_0}} \ln \frac{\tau_{k_0} + \tau_{f_i}}{\tau_{k_s} + \tau_{f_i}} - \frac{\tau_{f_j}}{\tau_{k_0}} \ln \frac{\tau_{k_0} + \tau_{f_j}}{\tau_{k_s} + \tau_{f_j}} \right|^{1/2} v_t & \text{for } \tau_{f_i}, \tau_{f_j} \leq \tau_{k_s}, \end{cases} \quad (25)$$

where τ_{f_i} is the friction time between the gas and dust particles with a radius a_i , that is, $\tau_f = 1/D_g$ for $a = a_i$. The times of $\tau_{k_0} (= \tau_{\text{eddy}} = 1/\Omega_K)$ and $\tau_{k_s} = Re^{-1/2}\tau_{k_0}$ are the turnover

times of the largest (l_t) and smallest ($Re^{-3/4}l_t$) turbulent eddies, respectively. The Reynolds number, Re , is estimated as

$$Re = v_t l_t / \nu = \alpha c_s H / \nu = 2 \times 10^{11} (R/\text{AU})^{-3/2} \alpha, \quad (26)$$

where we adopt the molecular viscosity of $\nu = c_s l_g / 3 = (c_s m_\mu) / (3\sigma_{\text{mol}} \rho_{\text{gas}})$ (e.g., Jeans 1916). In this work we calculate the dust evolution in a weakly and strongly turbulent disk, in which we adopt $\alpha = 10^{-4}$ ($v_t = 10^{-2} c_s$ and $l_t = 10^{-2} H$) and $\alpha = 10^{-2}$ ($v_t = 10^{-1} c_s$ and $l_t = 10^{-1} H$), respectively.

As the mass transport of dust particles in the vertical direction, we take into account the transport due to turbulent mixing as we mentioned in §2.3. If we separate the particle mass density and the velocity into mean and fluctuating parts, the mass flux in the second term of the left hand side of equation (12) is described as $V_Z(i) \cdot \varphi(i) = \overline{V_Z(i)} \cdot \overline{\varphi(i)} + \overline{V'_Z(i)} \cdot \overline{\varphi'(i)}$, where the overline means a time average and the prime is a fluctuation due to the turbulent motion. As the mean vertical velocity we adopt $\overline{V_Z(i)} = -(\Omega_K^2 / D_g) Z$ (see §4.1). The second term of the right hand side of the equation, $\overline{V'_Z(i)} \cdot \overline{\varphi'(i)}$, is the correlation of the fluctuations and treated as turbulent mixing, following the gradient diffusion hypothesis; $\overline{V'_Z(i)} \cdot \overline{\varphi'(i)} = -D_0 [\partial \overline{\varphi(i)} / \partial z]$, which works so as to diffusively uniform the mass density gradient of $\varphi(i)$ (we omit the overline hereafter) in the vertical direction as the dust particles move around from eddy to eddy. For the diffusivity, we adopt $D_0 = v_t l_t / (1 + \tau_f / \tau_{\text{eddy}}) = \alpha c_s H / (1 + \Omega_K / D_g)$ (e.g., Cuzzi et al. 1993; Weidenschilling 1997). The equation (12) is, therefore, solved by adopting

$$V_Z(i) \cdot \varphi(i) = -\frac{\Omega_K^2}{D_g} Z \varphi(i) - D_0 \frac{\partial \varphi(i)}{\partial z} \quad (27)$$

for simulating the dust evolution in a turbulent disk.

In Figure 5 we plot the resulting time evolution of the surface density of the dust particles whose radii reach a_{crit} , $\Sigma(a > a_{\text{crit}}) = \int_{-H}^H dZ \sum_{i=i_{\text{crit}}}^n \varphi(i)$ (i_{crit} corresponds to a_{crit}), divided by the total dust surface density, Σ_{dust} (eq.[2]). As mentioned before, we have removed those large particles in the numerical simulation, taking into account the rapid radially inward migration. The figure shows that more than 70% of the total dust mass moves toward the central star very rapidly within about 70, 9×10^2 , and 1×10^4 yrs in a strongly turbulent disk ($\alpha = 10^{-2}$; solid lines), while about 5×10^2 , 3×10^3 , and 3×10^4 yrs in a weakly turbulent disk ($\alpha = 10^{-4}$; dashed lines), at the orbits of $R = 1, 5.2$, and 30 AU, respectively. The timescale of the dust size growth is shorter at the inner disk where the particle density is higher.

Figure 6 shows the resulting size distributions of mass density of dust particles, $\varphi(i)$, normalized by $\rho_{\text{dust},0}$ at (a) $R = 1\text{AU}$, $t = 70$ yr, (b) $R = 5.2\text{AU}$, $t = 9 \times 10^2$ yr, and (c)

$R = 30\text{AU}$, $t = 1 \times 10^4$ yr, in a strongly turbulent disk ($\alpha = 10^{-2}$). Figure 7 is the same as Figure 6, but in a weakly turbulent disk ($\alpha = 10^{-4}$), at (a) $R = 1\text{AU}$, $t = 5 \times 10^2$ yr, (b) $R = 5.2\text{AU}$, $t = 3 \times 10^3$ yr, and (c) $R = 30\text{AU}$, $t = 3 \times 10^4$ yr. We note that the normalization factor in Figures 6 and 7 is different from that in Figure 3; $\rho_{\text{dust},0}$ used in Figures 6 and 7 is the initial dust density, $\rho_{\text{dust},0} = 4.2 \times 10^{-3} \rho_{\text{gas}}$ and $1.8 \times 10^{-2} \rho_{\text{gas}}$ for $R < 2.7\text{AU}$ and $R > 2.7\text{AU}$, respectively, while ρ_{dust} used in Figure 3 is the dust density at a specific time and spatial position defined in equation (14). The thick solid, dashed, and dot-dashed lines in each figure represent the size distributions at $Z = H$, $0.5H$, and $0.1H$, respectively. The time used in the figures is when 70% of the dust particles grow large enough to migrate toward the central star very rapidly at each orbit, R (see Fig. 5). We can see from the figures that at each orbit, R , the size distributions of smaller dust particles are almost identical at each height, while those of larger particles are very different. In the strongly turbulent disk ($\alpha = 10^{-2}$; Fig. 6) the smaller particles have similar size distributions at each height mainly because the turbulence induced motion dominates the relative velocity and the dust size growth (e.g., Weidenschilling 1984) in almost all disk heights, Z ; i.e., $\delta V \simeq \delta V_t$ independent of Z . Meanwhile, in the weakly turbulent disk ($\alpha = 10^{-4}$; Fig. 7) the differential vertical velocity, δV_Z , dominates the relative velocity at $Z \approx H$ where the gravitational force in the vertical direction is strong, while the turbulence induced relative velocity, δV_t , is dominant near the disk midplane. Therefore, the dust particles grow more rapidly at the disk surface, $Z \approx H$, and small particles are replenished from lower disk layers via the turbulent mixing, which works so as to uniform $\varphi(i)$. Consequently, the size distributions of smaller particles are not very different at each height also in the weakly turbulent disk. While the diffusive motion of turbulent mixing is strong enough to prevent the settling for the smaller particles, the larger particles cannot be sustained because of weak coupling with the gas and settle toward the disk midplane. So, the larger particles near the disk surface deplete as we can see from the figures. The depletion is more remarkable in the weakly turbulent disk (e.g., Dubrulle et al. 1995; Cuzzi et al. 1996; Cuzzi & Weidenschilling 2005). The gaps appear around $a = (7, 4, \text{ and } 1.1)\alpha^{-1/2}\mu\text{m}$ at $R = 1, 5.2, \text{ and } 30\text{AU}$, respectively, in Figures 6 and 7, owing to the discontinuities of the approximate treatment of the turbulence induced relative motion at $\tau_f = \tau_{k_s}$ (see eq. [25]).

Our result that the most dust particles migrate toward the central star at a very short timescale suggests that global turbulent motion should cease for the planetesimal formation in protoplanetary disks. Unless the strength of turbulence is weak, the density of dust particles around the disk midplane will be low enough because of the turbulent stirring so that they cannot collisionally grow into planetesimals, as has been noted also by some previous works (e.g., Stepinski & Valageas 1996; Cuzzi & Zahnle 2004; Weidenschilling 2004; Cuzzi & Weidenschilling 2005). In a quiescent disk the dust particles will settle toward the

disk midplane and form a dust layer in a sufficiently short timescale as we have seen in the previous section. Afterwards the shear between the dust layer and the gas will cause a local turbulent motion near the midplane. Detailed analysis of the evolution of dust particles in such a turbulent dust layer, although it is beyond a scope of this work, is in progress for further understanding of the planetesimal formation process (e.g., Goldreich & Ward 1973; Cuzzi et al. 1993; Weidenschilling 1995; Sekiya 1998; Ishitsu & Sekiya 2003; Youdin & Shu 2002; Weidenschilling 2003; Youdin & Chiang 2004).

5. Summary

We have investigated the dust size growth and settling toward the disk midplane in a quiescent or turbulent protoplanetary disk by numerically solving coagulation equation for settling dust particles.

Our result shows that the dust particles settle toward the disk midplane to form a gravitationally unstable layer at a short timescale (2×10^3 – 4×10^4 yr at $R = 1$ – 30 AU) if we assume an ideally quiescent disk. The radii of the largest dust particles just before the formation of the unstable layer are 20–1 cm at 1–30 AU. The resulting settling time and evolution of the largest dust radius in our numerical simulation are in good agreement with those obtained by the analytic calculation in NSH86, although they did not take into account the dust size distribution explicitly. This is because most dust mass is included in the dust particles with the largest sizes, and these particles control the dust settling time.

Also, we have discussed the dust evolution in an opposite extreme case of a globally turbulent disk to find that the dust particles are forced to fluctuate by turbulent motion of the gas, and grow to be large enough (32–6 cm at 1–30AU) to move inward very rapidly within a short timescale (70 – 3×10^4 yr at 1–30 AU). Thus, our result suggests that the disk should be quiescent or the global turbulent motion should cease before most mass of dust particles accrete onto the central star, in order to form planetesimals in protoplanetary disks. Self-consistent treatment of the evolution of the globally turbulent regions and the dust evolution processes is needed in future work. In addition, the dust evolution in a locally turbulent motion induced by the shear between the dust layer and the gas near the disk midplane should be investigated for further understanding of the planetesimal formation process.

We would like to thank the referee, Dr. S.J. Weidenschilling for his comments which were greatly helpful in improving our paper. Also, we are grateful to Makoto Kohno for arranging the numerical code for coagulation of settling dust particles. This work is supported by “The 21st Century COE Program of Origin and Evolution of Planetary Systems” and the

Grants-in-Aid for Scientific Research 17540217, 17039008, and 16036205 in MEXT.

A. Testing Numerical Solution of Coagulation Equation

It is known that a numerical calculation of coagulation equation with inappropriate conditions, for example, coarse mass bins, causes some serious errors like an artificial acceleration of coagulation that could lead to an artificial runaway (e.g., Ohtsuki et al. 1990; Wetherill 1990). Here we test our numerical solution of coagulation equation by comparing it with an analytic solution, using different numerical conditions. A linear kernel of $m_i m_j \beta(i, j) = Q(m_i + m_j)$ (Q is a constant) is used as a coalescence rate. In this case the coagulation equation with an initial condition of $\varphi(i)/(m_i/m_1)^2|_{t=0} = \rho_{\text{dust}} e^{-m_i/m_1}$ has an analytic solution,

$$\frac{\varphi(i)}{(m_i/m_1)^2} = \frac{\rho_{\text{dust}} \exp[-\eta + (m_i/m_1)(2 - e^{-\eta})]}{(m_i/m_1)(1 - e^{-\eta})^{1/2}} I_1[2(m_i/m_1)(1 - e^{-\eta})^{1/2}] \quad (\text{A1})$$

$$\approx \frac{\rho_{\text{dust}} \exp\{-\eta - (m_i/m_1)[1 - (1 - e^{-\eta})^{1/2}]^2\}}{2\pi^{1/2}(m_i/m_1)^{3/2}(1 - e^{-\eta})^{3/4}} \quad (\text{A2})$$

where $I_1(x)$ is the modified Bessel function and $\eta = Q\rho_{\text{dust}}t$ (Safronov 1963, 1969).

In Figure 8 we compare the analytic solutions (A2) (solid lines) and the numerical solutions (crosses) which have an initial condition for the dust mass distributing at m_1 . The mass distributions divided by ρ_{dust} at $\eta = 3, 6, 9,$ and 12 are plotted. Different numerical conditions are used in each figure; (a) $\varepsilon = \sqrt{2}$, $\varphi_{\text{min}} = 0$, (b) $\varepsilon = \sqrt[4]{2}$, $\varphi_{\text{min}} = 0$, and (c) $\varepsilon = \sqrt[4]{2}$, $\varphi_{\text{min}} = 10^{-21}\rho_{\text{dust}}$, where ε is the intervals of the dust mass bins, $m_{i+1/2} = \varepsilon m_{i-1/2}$ (see §2.3), and we prohibit the collisional coagulation ($\beta(i, j) = 0$) if $\varphi(i) < \varphi_{\text{min}}$ or $\varphi(j) < \varphi_{\text{min}}$ (e.g., Ohtsuki et al. 1990). In this paper we choose the conditions $\varepsilon = \sqrt[4]{2}$ and $\varphi_{\text{min}} = 10^{-21}\rho_{\text{dust}}$, with which the numerical solution is unlikely to cause the artificial runaway.

REFERENCES

- Adachi, I., Hayashi, C., & Nakazawa, K. 1976, *Prog. Theor. Phys.*, 56, 1756
- Aikawa, Y., & Nomura, H. 2005, submitted to *ApJ*
- Aikawa, Y., van Zadelhoff, G. J., van Dishoeck, E. F., & Herbst, E. 2002, *A&A*, 386, 622
- Balbus, S.A., & Hawley, J.F. 1991, *ApJ*, 376, 214

- Beckwith, S. V. W., & Sargent, A. I. 1991, *ApJ*, 381, 250
- Beckwith, S.V.W., Henning, T., & Nakagawa, Y. 2000 in *Protostars and Planets IV*, ed. V.G. Mannings, A.P. Boss, & S.S. Russell (Tucson: Univ. Arizona Press), 533
- Chandrasekhar, S. 1961, *Hydrodynamic and Hydromagnetic Stability* (Oxford: Oxford Univ. Press)
- Chiang, E. I., & Goldreich, P. 1997, *ApJ*, 490, 368
- Cuzzi, J. N., Dobrovolskis, A. R., & Champney, J. M. 1993, *Icarus*, 106, 102
- Cuzzi, J. N., Dobrovolskis, A. R., & Hogan, R. C. 1996, in *Chondrules and the Protoplanetary Disk*, ed. R.H. Hewins, R.H. Jones, & E.R.D. Scott (Cambridge; New York: Cambridge Univ. Press), 35
- Cuzzi, J.N., Hogan, R.C., Paque, J.M., & Dobrovolskis, A.R. 2001, *ApJ*, 546, 496
- Cuzzi, J. N. & Weidenschilling, S. J. 2005, in *Meteorites and the Early Solar System II*, ed. D.S. Lauretta & H.Y. McSween Jr. (Tucson: Univ. Arizona Press), in press
- Cuzzi, J.N. & Zahnle, K.J. 2004, *ApJ*, 614, 490
- D'Alessio, P., Calvet, N., & Hartmann, L. 2001, *ApJ*, 553, 321
- D'Alessio, P., Cantó, J., Calvet, N., & Lizano, S. 1998, *ApJ*, 500, 411
- Dubrulle, B., Morfill, G., & Sterzik, M. 1995, *Icarus*, 114, 237
- Dullemond, C. P. & Dominik, C. 2005, *A&A*, 434, 971
- Dullemond, C.P., Dominik, C., & Natta, A. 2001, *ApJ*, 560, 957
- Epstein, P.S. 1924, *Phys. Rev*, 23, 710
- Goldreich, P., & Ward, W. R. 1973, *ApJ*, 183, 1051
- Hayashi, C. 1981, *Prog. Theor. Phys. Suppl.*, 70, 35
- Hayashi, C., Nakazawa, K., & Nakagawa, Y. 1985, in *Protostars and Planets II*, ed. D.C. Black & M.S. Mathews (Tucson: Univ. Arizona Press), 1100
- Ishitsu, N., & Sekiya, M. 2003, *Icarus*, 165, 181
- Jeans, J.H. 1916, *The Dynamical Theory of Gases* (Cambridge: University Press)

- Johansen, A., Andersen, A.C., & Brandenburg, A. 2004, *A&A*, 417, 361
- Kenyon, S. J., & Hartmann, L. 1987, *ApJ*, 323, 714
- Kitamura, Y., Momose, M., Yokogawa, S., Kawabe, R., Tamura, M., & Ida, S. 2002, *ApJ*, 581, 357
- Klahr, H. H., & Henning, T. 1997, *Icarus*, 128, 213
- Landau, L.D., Akhiezer, A.I., & Lifshitz, E.M. 1967, *General Physics* (Oxford; New York: Pergamon Press)
- Landau, L.D. & Lifshitz, E.M. 1959, *Fluid Mechanics* (Oxford: Pergamon Press)
- Lin, D.N.C., & Papaloizou, J.C.B. 1980, *MNRAS*, 191, 37
- Markiewicz, W.J., Mizuno, H., & Völk, H.J. 1991, *A&A*, 242, 286
- Miyake, K., & Nakagawa, Y. 1993, *Icarus*, 106, 20
- Miyake, K., & Nakagawa, Y. 1995, *ApJ*, 441, 361
- Mizuno, H., Markiewicz, W. J., & Völk, H. J. 1988, *A&A*, 195, 183
- Nakagawa, Y., & Kohno, M. 1999, *AAS Div. Planet. Sci. Meeting*, 31, 1003
- Nakagawa, Y., Nakazawa, K., & Hayashi, C. 1981, *Icarus*, 45, 517
- Nakagawa, Y., Sekiya, M., & Hayashi, C. 1986, *Icarus*, 67, 375 (NSH86)
- Nomura, H. 2004, *Ap&SS*, 292, 435
- Nomura, H. & Millar, T.J. 2005, *A&A*, 438, 923
- Ohtsuki, K., Nakagawa, Y., & Nakazawa, K. 1990, *Icarus*, 83, 205
- Oppenkopf, V. 1993, *A&A*, 280, 617
- Przygodda, F., van Boekel, R., Abraham, P., Melnikov, S.Y., Waters, L.B.F.M., & Leinert, Ch. 2003, *A&A*, 412, L43
- Safronov, V.S. 1963, *Sov. Phys. Dokl.*, 7, 967
- Safronov, V.S. 1969, *Evolution of the Protoplanetary Cloud and Formation of the Earth and Planets* (Moscow: Nauka Press)

- Sano, T., Miyama, S.M., Umebayashi, T., & Nakano, T. 2000, *ApJ*, 543, 486
- Sekiya, M. 1998, *Icarus*, 133, 298
- Stepinski, T. F. & Valageas, P. 1996, *A&A*, 309, 301
- Stokes, G.G. 1851, *Trans. Camb. Phil. Soc.*, 9, Pt.II, 8
- Suttner, G., & Yorke, H. W. 2001, *ApJ*, 551, 461
- Tanaka, H., Himeno, Y., & Ida, S. 2005, *ApJ*, 625, 414
- van Boekel, R., Waters, L. B. F. M., Dominik, C., Bouwman, J. de Koter, A. Dullemond, C.P., & Paresce, F. 2003, *A&A*, 400, L21
- van Zadelhoff, G.-J., van Dishoeck, E.F., Thi, W.-F., & Blake, G. A. 2001, *A&A*, 377, 566
- Völk, H. J., Morfill, G. E., Roeser, S., & Jones, F. C. 1980, *A&A*, 85, 316
- Weidenschilling, S. J. 1980, *Icarus*, 44, 172
- Weidenschilling, S. J. 1984, *Icarus*, 60, 553
- Weidenschilling, S. J. 1995, *Icarus*, 116, 433
- Weidenschilling, S. J. 1997, *Icarus*, 127, 290
- Weidenschilling, S. J. 2003, *Icarus*, 165, 438
- Weidenschilling, S. J. 2004, in *Comets II*, ed. C. Festou, H. U. Keller, & H. A. Weaver (Tucson: Univ. Arizona Press), 97
- Weidenschilling, S. J., & Cuzzi, J. N. 1993, in *Protostar and Planets III*, ed. E. H. Levy & J. L. Lunine (Tucson: Univ. Arizona Press), 1031
- Wetherill, G.W. 1990, *Icarus*, 88, 336
- Wilner, D.J., D'Alessio, P., Calvet, N., Claussen, M.J., & Hartmann, L. 2005, *ApJ*, 626, L109
- Youdin, A. N. & Shu, F. H. 2002, *ApJ*, 580, 494
- Youdin, A.N. & Chiang, E.I. 2004, *ApJ*, 601, 1109

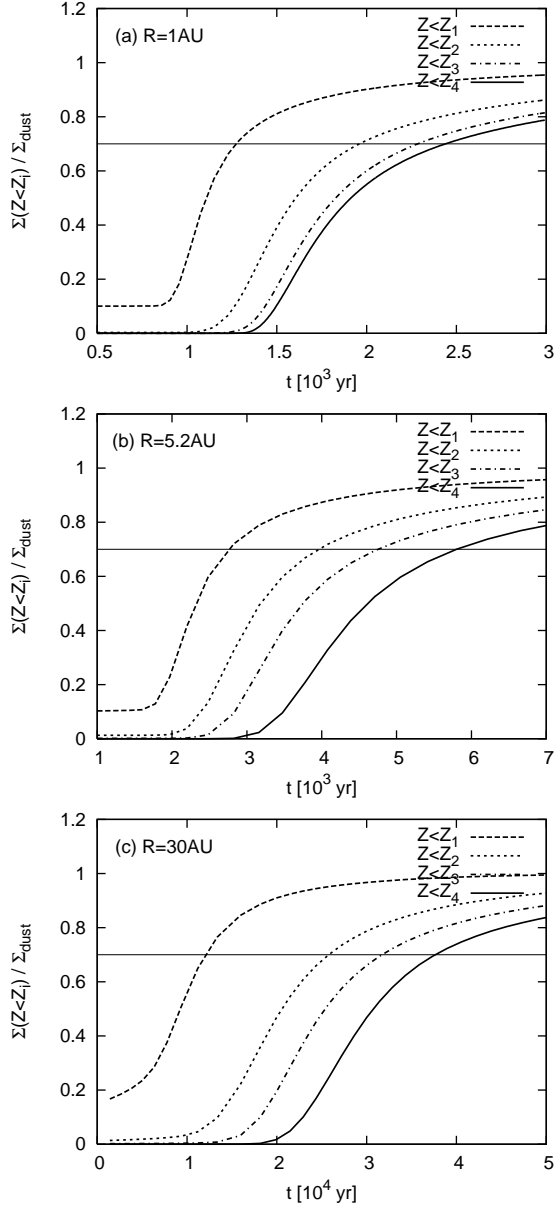


Fig. 1.— The time evolution of spatial dust mass distribution obtained by our numerical calculation at the orbits of $R =$ (a) 1AU, (b) 5.2AU, and (c) 30AU. The dashed, dotted, dot-dashed, and solid lines represent the dust surface density below the characteristic heights, $Z = Z_1, Z_2, Z_3,$ and $Z_4,$ respectively, divided by the total dust surface density, Σ_{dust} . The thin solid lines at $\Sigma(Z < Z_i)/\Sigma_{\text{dust}} = 0.7$ are used in order to estimate the dust settling time in Figure 2.

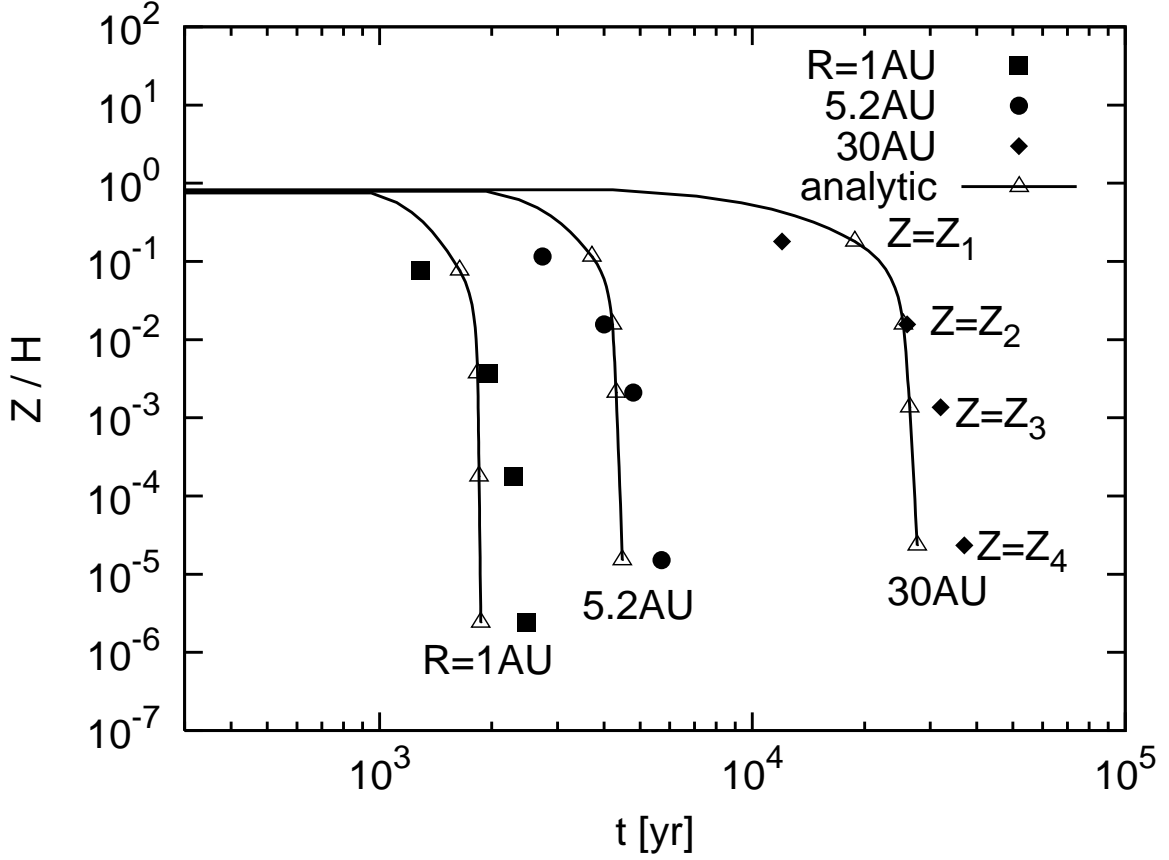


Fig. 2.— The dust settling time at the characteristic height $Z = Z_i$ ($i = 1, \dots, 4$) and $R = 1\text{AU}$ (squares), 5.2AU (circles), and 30AU (diamonds), obtained by our numerical calculation. The dust settling time by NSH86 is also plotted (triangles with solid lines). The numerical results are in good agreement with the analytic results, and most dust particles settle below $Z = Z_4$, within about 2×10^3 , 5×10^3 , and 3×10^4 yrs at the orbits of $R = 1$, 5.2 , and 30AU , respectively, in a quiescent disk.

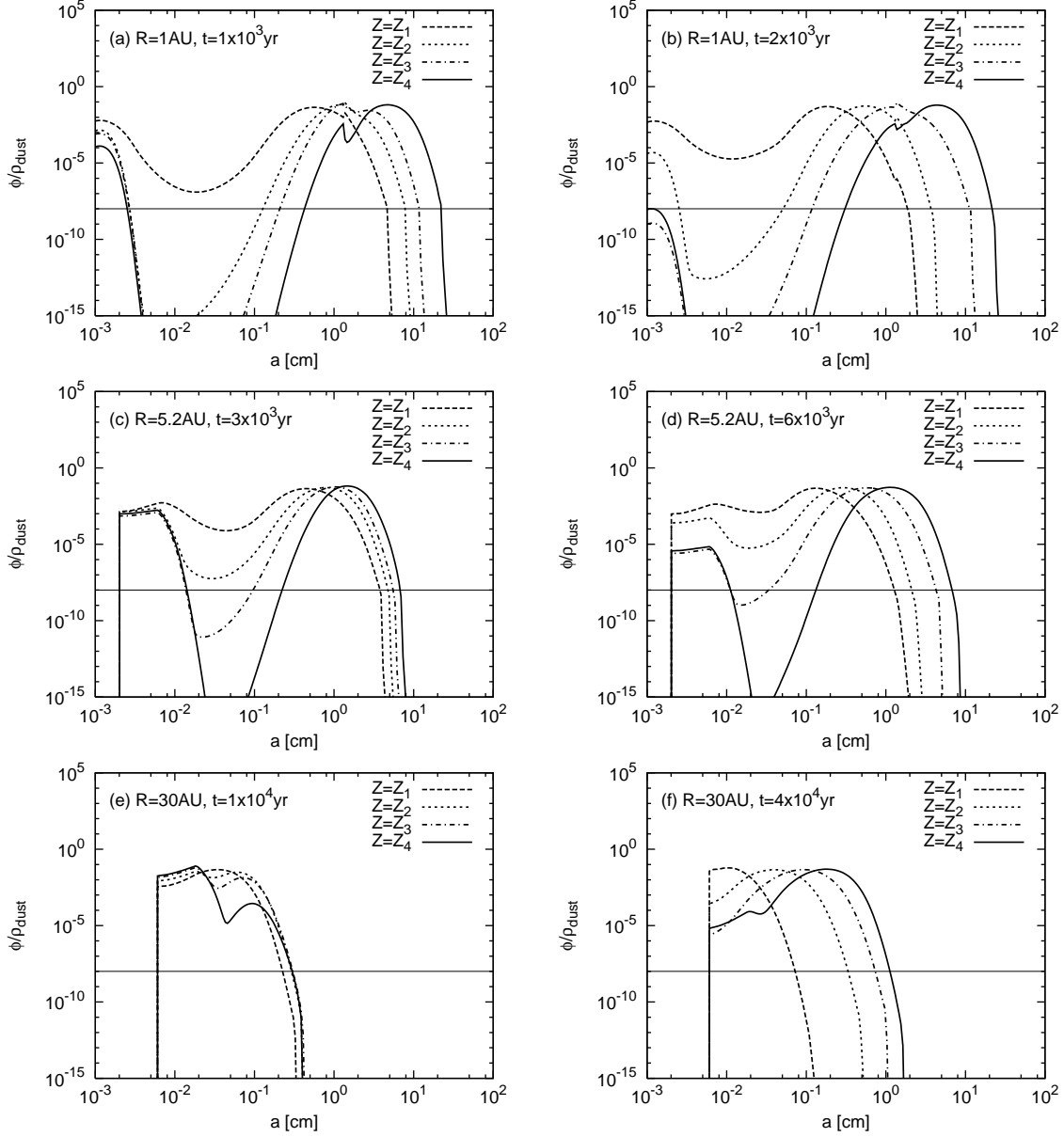


Fig. 3.— The size distributions of mass density of dust particles, $\varphi(i)$, normalized by ρ_{dust} at each orbit, R , and time, t , in a quiescent disk. The dashed, dotted, dot-dashed, and solid lines represent the size distributions at the characteristic heights $Z = Z_1, Z_2, Z_3$, and Z_4 , respectively. The thin solid lines at $\varphi/\rho_{\text{dust}} = 10^{-8}$ are used as a criterion to estimate the largest dust radii in Figure 4.

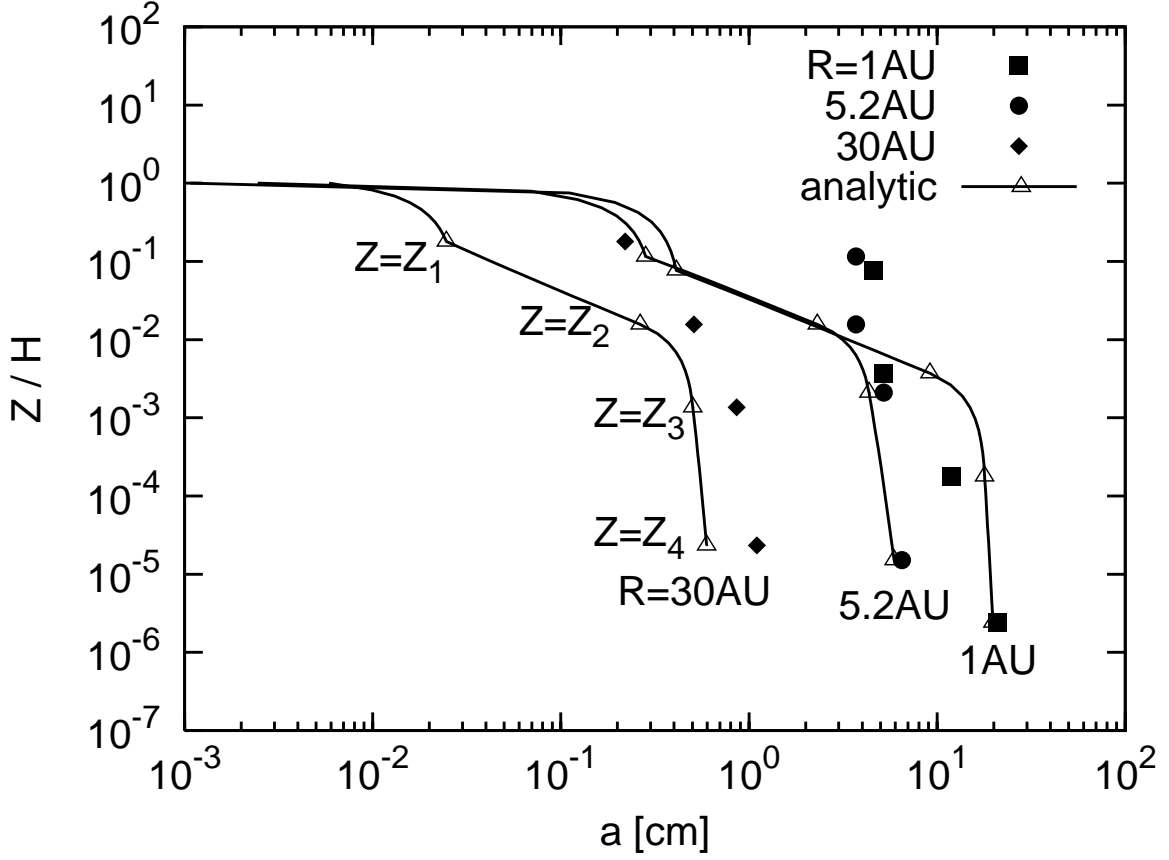


Fig. 4.— The largest dust radii at the characteristic height $Z = Z_i$ ($i = 1, \dots, 4$) and $R = 1\text{AU}$ (squares), 5.2AU (circles), and 30AU (diamonds), obtained by our numerical calculation. The evolution of dust radii by NSH86 is also plotted (triangles with solid lines). The numerical results are in good agreement with the analytic results within a factor of two, except at $Z = Z_1$, and the dust radius finally reaches about 20, 7, and 1 cm at the orbits of $R = 1, 5.2$, and 30AU , respectively, just before most dust particles settle below $Z = Z_4$.

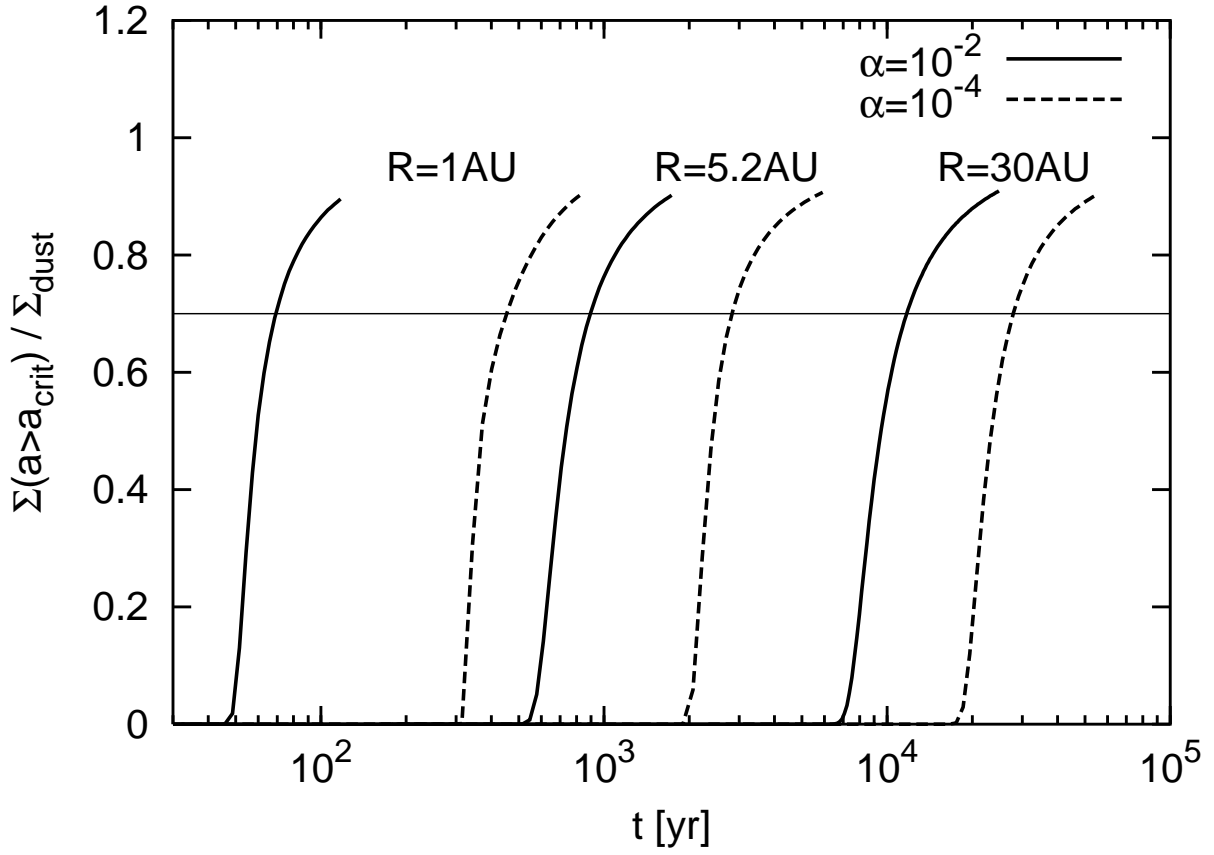


Fig. 5.— The time evolution of the surface density of the dust particles which are larger than a_{crit} in strongly ($\alpha = 10^{-2}$; solid lines) and weakly ($\alpha = 10^{-4}$; dashed lines) turbulent disks. Most mass of dust particles is included in large particles, which can migrate toward the central star, at a very short timescale ($\sim 70\text{--}3 \times 10^4\text{yr}$ at 1–30 AU).

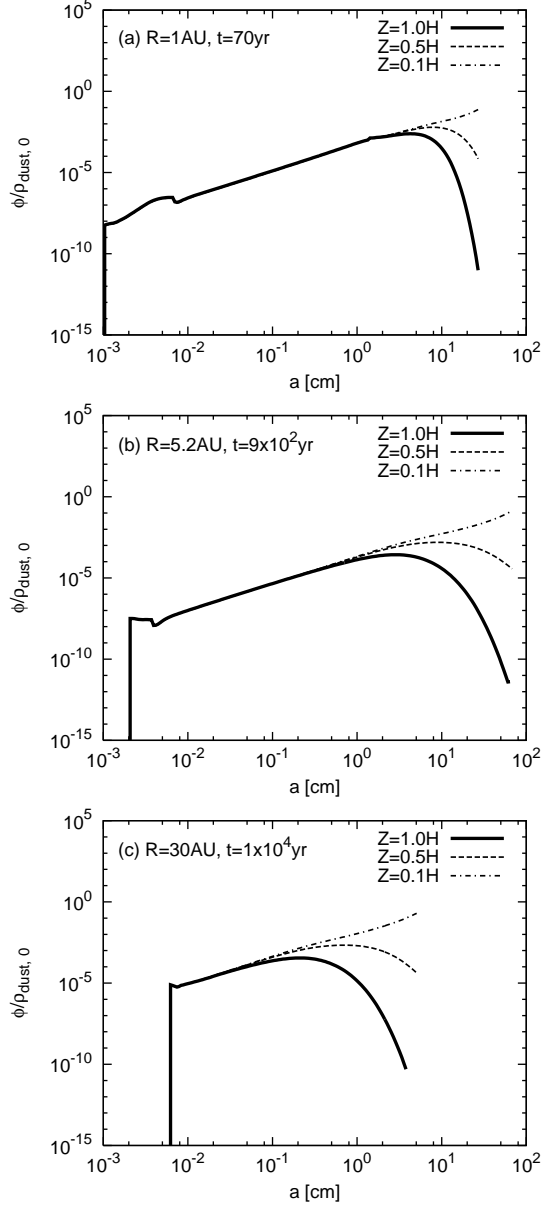


Fig. 6.— The size distributions of mass density of dust particles, $\varphi(i)$, normalized by $\rho_{\text{dust},0}$ at each orbit, R , and time, t in a strongly turbulent disk ($\alpha = 10^{-2}$). Note that the normalization factor is different from Figure 3 (see text). The thick solid, dashed, and dot-dashed lines represent the size distributions at $Z = H$, $0.5H$, and $0.1H$, respectively. The size distributions of smaller dust particles are almost identical at each height mainly because the turbulence induced motion dominates the relative velocity in almost all regions. Larger particles near the disk surface deplete since the turbulent diffusion against the settling toward the disk midplane is not strong due to weak coupling with the gas motion.

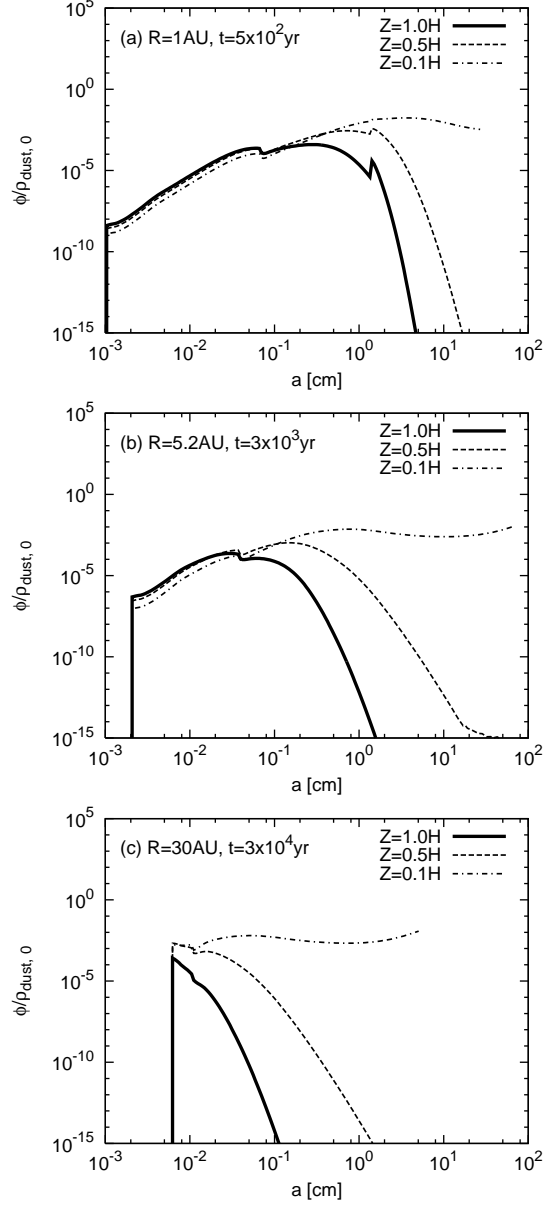


Fig. 7.— The same as Figure 6, but in a weakly turbulent disk ($\alpha = 10^{-4}$). The size distributions of smaller dust particles are not very different at each height because of the turbulent mixing in the vertical direction. The depletion of larger particles at the upper disk layer is more remarkable than that in the strongly turbulent disk.

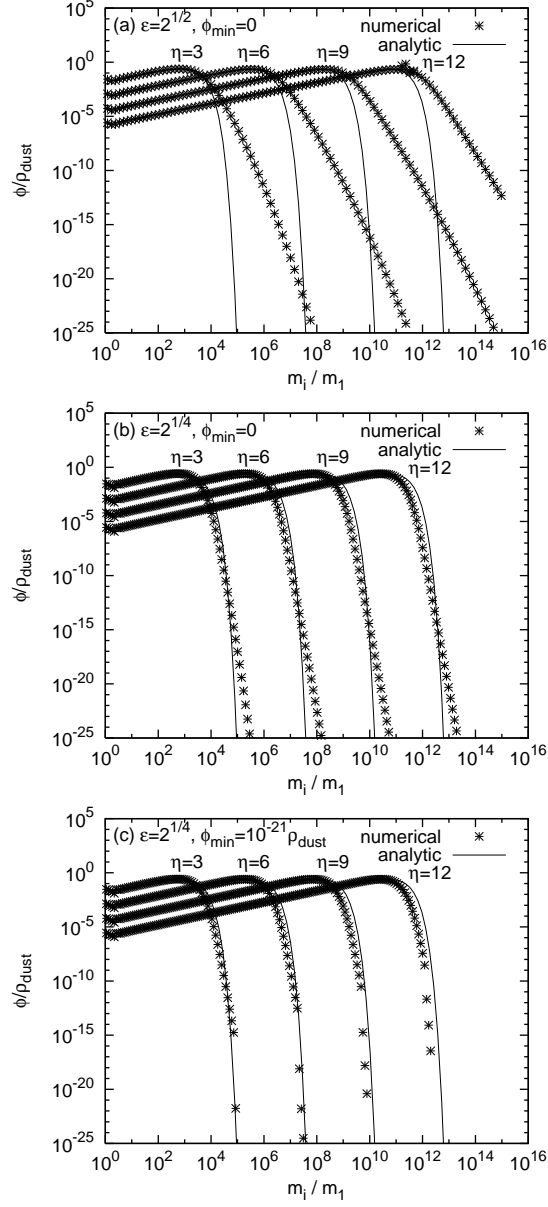


Fig. 8.— Analytic (solid lines) and numerical (crosses) solutions for the mass distributions at $\eta = 3, 6, 9,$ and 12 . Different numerical conditions are used in each figure; (a) $\varepsilon = \sqrt{2}$, $\varphi_{\text{min}} = 0$, (b) $\varepsilon = \sqrt[4]{2}$, $\varphi_{\text{min}} = 0$, and (c) $\varepsilon = \sqrt[4]{2}$, $\varphi_{\text{min}} = 10^{-21}\rho_{\text{dust}}$. The conditions $\varepsilon = \sqrt[4]{2}$ and $\varphi_{\text{min}} = 10^{-21}\rho_{\text{dust}}$ are used in this paper.

Table 1. Characteristic Disk Heights

	$R = 1\text{AU}$	$R = 5.2\text{AU}$	$R = 30\text{AU}$
Z_1/H	7.7×10^{-2}	1.2×10^{-1}	1.8×10^{-1}
Z_2/H	3.7×10^{-3}	1.6×10^{-2}	1.6×10^{-2}
Z_3/H	1.8×10^{-4}	2.1×10^{-3}	1.4×10^{-3}
Z_4/H	2.4×10^{-6}	1.5×10^{-5}	2.4×10^{-5}
H [AU]	4.7×10^{-2}	3.7×10^{-1}	3.3